Research Article | Vol. 24, No. 23 | 14 Nov 2016 | OPTICS EXPRESS 26777

Optics EXPRESS

Towards unsupervised fluorescence lifetime imaging using low dimensional variable projection

YONGLIANG ZHANG,[1,2] ANNIE CUYT,[3] WEN-SHIN LEE,[3] GIOVANNI LO BIANCO,[4] GANG WU,[5] YU CHEN,[6] AND DAVID DAY-UEI LI[1,*]

[1]*Centre for Biophotonics, Strathclyde Institute of Pharmacy and Biomedical Sciences, University of Strathclyde, Glasgow G4 0RE, Scotland, UK*
[2]*College of Information Science & Electronic Engineering, Zhejiang University, Hangzhou 310007, China*
[3]*Department of Mathematics and Computer Science, University of Antwerp, Antwerp 2020, Belgium*
[4]*Computer Science for Decision Support, École des Mines de Nantes, Nantes 44307, France*
[5]*School of Engineering and Informatics, University of Sussex, Brighton BN1 9QT, UK*
[6]*Department of Physics, University of Strathclyde, Glasgow G4 0NG Scotland, UK*
**David.Li@strath.ac.uk*

Abstract: Analyzing large fluorescence lifetime imaging (FLIM) data is becoming overwhelming; the latest FLIM systems easily produce massive amounts of data, making an efficient analysis more challenging than ever. In this paper we propose the combination of a custom-fit variable projection method, with a Laguerre expansion based deconvolution, to analyze bi-exponential data obtained from time-domain FLIM systems. Unlike nonlinear least squares methods, which require a suitable initial guess from an experienced researcher, the new method is free from manual interventions and hence can support automated analysis. Monte Carlo simulations are carried out on synthesized FLIM data to demonstrate the performance compared to other approaches. The performance is also illustrated on real-life FLIM data obtained from the study of autofluorescence of daisy pollen and the endocytosis of gold nanorods (GNRs) in living cells. In the latter, the fluorescence lifetimes of the GNRs are much shorter than the full width at half maximum of the instrument response function. Overall, our proposed method contains simple steps and shows great promise in realising automated FLIM analysis of large data sets.

OCIS codes: (030.5260) Photon counting; (110.2960) Image analysis; (110.0180) Microscopy; (100.1830) Deconvolution; (170.3650) Lifetime-based sensing; (170.6920) Time-resolved imaging.

References and links

1. A. Shivalingam, M. A. Izquierdo, A. Le Marois, A. Vyšniauskas, K. Suhling, M. K. Kuimova, and R. Vilar, "The interactions between a small molecule and G-quadruplexes are visualized by fluorescence lifetime imaging microscopy," Nat. Commun. **6**, 8178 (2015).
2. D. Fixler, "Fluorescence Imaging for Biomedical Analysis," in *The Optics Encyclopedia* (Wiley-VCH Verlag GmbH & Co., 2015).
3. G. O. Fruhwirth, L. P. Fernandes, G. Weitsman, G. Patel, M. Kelleher, K. Lawler, A. Brock, S. P. Poland, D. R. Matthews, G. Kéri, P. R. Barber, B. Vojnovic, S. M. Ameer-Beg, A. C. C. Coolen, F. Fraternali, and T. Ng, "How Förster resonance energy transfer imaging improves the understanding of protein interaction networks in cancer biology," ChemPhysChem **12**(3), 442–461 (2011).
4. K. Okabe, N. Inada, C. Gota, Y. Harada, T. Funatsu, and S. Uchiyama, "Intracellular temperature mapping with a fluorescent polymeric thermometer and fluorescence lifetime imaging microscopy," Nat. Commun. **3**, 705 (2012).
5. M. Nobis, E. J. McGhee, J. P. Morton, J. P. Schwarz, S. A. Karim, J. Quinn, M. Edward, A. D. Campbell, L. C. McGarry, T. R. J. Evans, V. G. Brunton, M. C. Frame, N. O. Carragher, Y. Wang, O. J. Sansom, P. Timpson, and K. I. Anderson, "Intravital FLIM-FRET imaging reveals dasatinib-induced spatial control of src in pancreatic cancer," Cancer Res. **73**(15), 4674–4686 (2013).

#275434 http://dx.doi.org/10.1364/OE.24.026777
Journal © 2016 Received 7 Sep 2016; revised 19 Oct 2016; accepted 19 Oct 2016; published 10 Nov 2016

Optics EXPRESS

6. Y. Zhang, G. Wei, J. Yu, D. J. S. Birch, and Y. Chen, "Surface plasmon enhanced energy transfer between gold nanorods and fluorophores: application to endocytosis study and RNA detection," Faraday Discuss. **178**, 383–394 (2015).
7. S. Coda, A. J. Thompson, G. T. Kennedy, K. L. Roche, L. Ayaru, D. S. Bansi, G. W. Stamp, A. V. Thillainayagam, P. M. W. French, and C. Dunsby, "Fluorescence lifetime spectroscopy of tissue autofluorescence in normal and diseased colon measured ex vivo using a fiber-optic probe," Biomed. Opt. Express **5**(2), 515–538 (2014).
8. T. S. Blacker, Z. F. Mann, J. E. Gale, M. Ziegler, A. J. Bain, G. Szabadkai, and M. R. Duchen, "Separating NADH and NADPH fluorescence in live cells and tissues using FLIM," Nat. Commun. **5**, 3936 (2014).
9. D. M. Kavanagh, A. M. Smyth, K. J. Martin, A. Dun, E. R. Brown, S. Gordon, K. J. Smillie, L. H. Chamberlain, R. S. Wilson, L. Yang, W. Lu, M. A. Cousin, C. Rickman, and R. R. Duncan, "A molecular toggle after exocytosis sequesters the presynaptic syntaxin1a molecules involved in prior vesicle fusion," Nat. Commun. **5**, 5774 (2014).
10. Y. Sun, J. E. Phipps, J. Meier, N. Hatami, B. Poirier, D. S. Elson, D. G. Farwell, and L. Marcu, "Endoscopic fluorescence lifetime imaging for in vivo intraoperative diagnosis of oral carcinoma," Microsc. Microanal. **19**(4), 791–798 (2013).
11. S. R. Stürzenbaum, M. Höckner, A. Panneerselvam, J. Levitt, J. S. Bouillard, S. Taniguchi, L. A. Dailey, R. Ahmad Khanbeigi, E. V. Rosca, M. Thanou, K. Suhling, A. V. Zayats, and M. Green, "Biosynthesis of luminescent quantum dots in an earthworm," Nat. Nanotechnol. **8**(1), 57–60 (2012).
12. N. A. Hosny, G. Mohamedi, P. Rademeyer, J. Owen, Y. Wu, M.-X. Tang, R. J. Eckersley, E. Stride, and M. K. Kuimova, "Mapping microbubble viscosity using fluorescence lifetime imaging of molecular rotors," Proc. Natl. Acad. Sci. U.S.A. **110**(23), 9225–9230 (2013).
13. E. Gratton, S. Breusegem, J. Sutin, Q. Ruan, and N. Barry, "Fluorescence lifetime imaging for the two-photon microscope: time-domain and frequency-domain methods," J. Biomed. Opt. **8**(3), 381–390 (2003).
14. Y. Zhang, A. A. Khan, G. D. Vigil, and S. S. Howard, "Super-sensitivity multiphoton frequency-domain fluorescence lifetime imaging microscopy," Opt. Express **24**(18), 20862–20867 (2016).
15. H. Chen and E. Gratton, "A practical implementation of multifrequency widefield frequency-domain fluorescence lifetime imaging microscopy," Microsc. Res. Tech. **76**(3), 282–289 (2013).
16. G. Yahav, A. Hirshberg, O. Salomon, N. Amariglio, L. Trakhtenbrot, and D. Fixler, "Fluorescence lifetime imaging of DAPI-stained nuclei as a novel diagnostic tool for the detection and classification of B-cell chronic lymphocytic leukemia," Cytometry A **89**(7), 644–652 (2016).
17. H. A. R. Homulle, F. Powolny, P. L. Stegehuis, J. Dijkstra, D. U. Li, K. Homicsko, D. Rimoldi, K. Muehlethaler, J. O. Prior, R. Sinisi, E. Dubikovskaya, E. Charbon, and C. Bruschini, "Compact solid-state CMOS single-photon detector array for in vivo NIR fluorescence lifetime oncology measurements," Biomed. Opt. Express **7**(5), 1797–1814 (2016).
18. C. J. de Grauw and H. C. Gerritsen, "Multiple time-gate module for fluorescence lifetime imaging," Appl. Spectrosc. **55**(6), 670–678 (2001).
19. A. V. Agronskaia, L. Tertoolen, and H. C. Gerritsen, "Fast fluorescence lifetime imaging of calcium in living cells," J. Biomed. Opt. **9**(6), 1230–1237 (2004).
20. D. D. U. Li, J. Arlt, D. Tyndall, R. Walker, J. Richardson, D. Stoppa, E. Charbon, and R. K. Henderson, "Video-rate fluorescence lifetime imaging camera with CMOS single-photon avalanche diode arrays and high-speed imaging algorithm," J. Biomed. Opt. **16**(9), 096012 (2011).
21. J. L. Rinnenthal, C. Börnchen, H. Radbruch, V. Andresen, A. Mossakowski, V. Siffrin, T. Seelemann, H. Spiecker, I. Moll, J. Herz, A. E. Hauser, F. Zipp, M. J. Behne, and R. Niesner, "Parallelized TCSPC for dynamic intravital fluorescence lifetime imaging: quantifying neuronal dysfunction in neuroinflammation," PLoS One **8**(4), e60100 (2013).
22. R. M. Field, S. Realov, and K. L. Shepard, "A 100 fps, time-correlated single-photon-counting-based fluorescence-lifetime imager in 130 nm CMOS," IEEE J. Solid-St. Circulation **49**, 867–880 (2014).
23. M. G. Giacomelli, Y. Sheikine, H. Vardeh, J. L. Connolly, and J. G. Fujimoto, "Rapid imaging of surgical breast excisions using direct temporal sampling two photon fluorescent lifetime imaging," Biomed. Opt. Express **6**(11), 4317–4325 (2015).
24. S. P. Poland, N. Krstajić, J. Monypenny, S. Coelho, D. Tyndall, R. J. Walker, V. Devauges, J. Richardson, N. Dutton, P. Barber, D. D.-U. Li, K. Suhling, T. Ng, R. K. Henderson, and S. M. Ameer-Beg, "A high speed multifocal multiphoton fluorescence lifetime imaging microscope for live-cell FRET imaging," Biomed. Opt. Express **6**(2), 277–296 (2015).
25. K. Levenberg, "A method for the solution of certain non-linear problems in least squares," Q. Appl. Math. **2**, 164–168 (1944).
26. D. Marquardt, "An Algorithm for least-squares estimation of nonlinear parameters," SIAM J. Appl. Math. **11**(2), 431–441 (1963).
27. C. Y. Fu, B. K. Ng, and S. G. Razul, "Fluorescence lifetime discrimination using expectation-maximization algorithm with joint deconvolution," J. Biomed. Opt. **14**(6), 064009 (2009).
28. D.-U. Li, J. Arlt, J. Richardson, R. Walker, A. Buts, D. Stoppa, E. Charbon, and R. Henderson, "Real-time fluorescence lifetime imaging system with a 32 x 32 0.13 μm CMOS low dark-count single-photon avalanche diode array," Opt. Express **18**(10), 10257–10269 (2010).

Optics EXPRESS

29. D. D.-U. Li, S. Ameer-Beg, J. Arlt, D. Tyndall, R. Walker, D. R. Matthews, V. Visitkul, J. Richardson, and R. K. Henderson, "Time-domain fluorescence lifetime imaging techniques suitable for solid-state imaging sensor arrays," Sensors (Basel) **12**(12), 5650–5669 (2012).
30. S. P. Poland, A. T. Erdogan, N. Krstajić, J. Levitt, V. Devauges, R. J. Walker, D. D.-U. Li, S. M. Ameer-Beg, and R. K. Henderson, "New high-speed centre of mass method incorporating background subtraction for accurate determination of fluorescence lifetime," Opt. Express **24**(7), 6899–6915 (2016).
31. S. Padilla-Parra, N. Auduge, M. Coppey-Moisan, and M. Tramier, "Non fitting based FRET–FLIM analysis approaches applied to quantify protein–protein interactions in live cells," Biophys. Rev. **3**(2), 63–70 (2011).
32. A. Leray, S. Padilla-Parra, J. Roul, L. Héliot, and M. Tramier, "Spatio-Temporal Quantification of FRET in living cells by fast time-domain FLIM: a comparative study of non-fitting methods [corrected]," PLoS One **8**(7), e69335 (2013).
33. M. Elangovan, R. N. Day, and A. Periasamy, "Nanosecond fluorescence resonance energy transfer-fluorescence lifetime imaging microscopy to localize the protein interactions in a single living cell," J. Microsc. **205**(1), 3–14 (2002).
34. D. D.-U. Li, H. Yu, and Y. Chen, "Fast bi-exponential fluorescence lifetime imaging analysis methods," Opt. Lett. **40**(3), 336–339 (2015).
35. R. Niesner, B. Peker, P. Schlüsche, and K.-H. Gericke, "Noniterative biexponential fluorescence lifetime imaging in the investigation of cellular metabolism by means of NAD(P)H autofluorescence," ChemPhysChem **5**(8), 1141–1149 (2004).
36. K. C. Lee, J. Siegel, S. E. Webb, S. Lévêque-Fort, M. J. Cole, R. Jones, K. Dowling, M. J. Lever, and P. M. French, "Application of the stretched exponential function to fluorescence lifetime imaging," Biophys. J. **81**(3), 1265–1274 (2001).
37. J. R. Lakowicz, *Principles of Fluorescence Spectroscopy* (Springer, US, 2013).
38. J. A. Jo, Q. Fang, T. Papaioannou, J. D. Baker, A. H. Dorafshar, T. Reil, J.-H. Qiao, M. C. Fishbein, J. A. Freischlag, and L. Marcu, "Laguerre-based method for analysis of time-resolved fluorescence data: application to in-vivo characterization and diagnosis of atherosclerotic lesions," J. Biomed. Opt. **11**(2), 021004 (2006).
39. A. Agrawal, B. D. Gallas, C. Parker, K. M. Agrawal, and T. J. Pfefer, "Sensitivity of time-resolved fluorescence analysis methods for disease detection," IEEE J. Sel. Top. Quant. **16**(4), 877–885 (2010).
40. J. Liu, Y. Sun, J. Qi, and L. Marcu, "A novel method for fast and robust estimation of fluorescence decay dynamics using constrained least-squares deconvolution with Laguerre expansion," Phys. Med. Biol. **57**(4), 843–865 (2012).
41. P. Pande and J. A. Jo, "Automated analysis of fluorescence lifetime imaging microscopy (FLIM) data based on the Laguerre deconvolution method," IEEE Trans. Biomed. Eng. **58**(1), 172–181 (2011).
42. D. B. McCombie, A. T. Reisner, and H. H. Asada, "Laguerre-model blind system identification: cardiovascular dynamics estimated from multiple peripheral circulatory signals," IEEE Trans. Biomed. Eng. **52**(11), 1889–1901 (2005).
43. D. P. O'Leary and B. W. Rust, "Variable projection for nonlinear least squares problems," Comput. Optim. Appl. **54**(3), 579–593 (2013).
44. Y. Zhang, Y. Chen, and D. D.-U. Li, "Optimizing Laguerre expansion based deconvolution methods for analysing bi-exponential fluorescence lifetime images," Opt. Express **24**(13), 13894–13905 (2016).
45. G. H. Golub and V. Pereyra, "The differentiation of pseudo-inverses and nonlinear least squares problems whose variables separate," SIAM J. Numer. Anal. **10**(2), 413–432 (1973).
46. S. Laptenok, K. M. Mullen, J. W. Borst, I. H. van Stokkum, V. V. Apanasovich, and A. Visser, "Fluorescence lifetime imaging microscopy (FLIM) data analysis with TIMP," J. Stat. Softw. **18**(8), 1–20 (2007).
47. K. M. Mullen and I. H. Van Stokkum, "TIMP: an R package for modeling multi-way spectroscopic measurements," J. Stat. Softw. **18**(3), 1–46 (2007).
48. S. C. Warren, A. Margineanu, D. Alibhai, D. J. Kelly, C. Talbot, Y. Alexandrov, I. Munro, M. Katan, C. Dunsby, and P. M. French, "Rapid global fitting of large fluorescence lifetime imaging microscopy datasets," PLoS One **8**(8), e70687 (2013).
49. J. K. Barral, E. Gudmundson, N. Stikov, M. Etezadi-Amoli, P. Stoica, and D. G. Nishimura, "A robust methodology for in vivo T1 mapping," Magn. Reson. Med. **64**(4), 1057–1067 (2010).
50. Y. Zhang, D. J. S. Birch, and Y. Chen, "Two-photon excited surface plasmon enhanced energy transfer between DAPI and gold nanoparticles: Opportunities in intra-cellular imaging and sensing," Appl. Phys. Lett. **99**(10), 103701 (2011).
51. S. Pelet, M. J. R. Previte, L. H. Laiho, and P. T. C. So, "A fast global fitting algorithm for fluorescence lifetime imaging microscopy based on image segmentation," Biophys. J. **87**(4), 2807–2817 (2004).
52. P. Hall and B. Selinger, "Better estimates of exponential decay parameters," J. Phys. Chem. **85**(20), 2941–2946 (1981).
53. J. A. Jo, J. Park, P. Pande, S. Shrestha, M. J. Serafino, J. J. Rico Jimenez, F. Clubb, B. Walton, L. M. Buja, J. E. Phipps, M. D. Feldman, J. Adame, and B. E. Applegate, "Simultaneous morphological and biochemical endogenous optical imaging of atherosclerosis," Eur. Heart J. Cardiovasc. Imaging **16**(8), 910–918 (2015).
54. A. Draaijer, R. Sanders, and H. C. Gerritsen, "Fluorescence lifetime imaging, a new tool in confocal microscopy," in *Handbook of Biological Confocal Microscopy*, J. Pawley, ed. (Plenum Publishing, 1995), pp. 491–505.

Optics EXPRESS

55. P. R. Barber, S. M. Ameer-Beg, S. Pathmananthan, M. Rowley, and A. C. C. Coolen, "A Bayesian method for single molecule, fluorescence burst analysis," Biomed. Opt. Express **1**(4), 1148–1158 (2010).
56. M. Fritzsche and C.-F. Mandenius, "Fluorescent cell-based sensing approaches for toxicity testing," Anal. Bioanal. Chem. **398**(1), 181–191 (2010).
57. PicoQuant, http://www.picoquant.com/images/uploads/downloads/lifetime-fitting_using_the_flim-script_step_by_step.pdf.
58. G. Wu, T. Nowotny, Y. Zhang, H. Q. Yu, and D. D.-U. Li, "Artificial neural network approaches for fluorescence lifetime imaging techniques," Opt. Lett. **41**(11), 2561–2564 (2016).
59. D. Fixler, T. Nayhoz, and K. Ray, "Diffusion reflection and fluorescence lifetime imaging microscopy study of fluorophore-conjugated gold nanoparticles or nanorods in solid phantoms," ACS Photonics **1**(9), 900–905 (2014).
60. K. Saha, S. S. Agasti, C. Kim, X. Li, and V. M. Rotello, "Gold nanoparticles in chemical and biological sensing," Chem. Rev. **112**(5), 2739–2779 (2012).
61. G. Wei, J. Yu, J. Wang, P. Gu, D. J. Birch, and Y. Chen, "Hairpin DNA-functionalized gold nanorods for mRNA detection in homogenous solution," J. Biomed. Opt. **21**(9), 097001 (2016).
62. P. Tinnefeld, V. Buschmann, D.-P. Herten, K.-T. Han, and M. Sauer, "Confocal fluorescence lifetime imaging microscopy (FLIM) at the single molecule level," Single Mol. **1**(3), 215–223 (2000).

1. Introduction

Fluorescence lifetime imaging (FLIM) techniques are much more informative than the intensity based counterparts. Not only can FLIM microscopy sense the fluorescence intensity of fluorescent molecules (fluorophores), but it also can measure the decay rate (or lifetime) of the fluorescence. As fluorescence lifetimes of fluorophores are sensitive to the cellular microenvironments, FLIM is suitable for detecting physiological or electrochemical parameters such as Ca^{2+}, pH, O_2, or temperature. When combined with Förster resonance energy transfer (called FLIM-FRET), it is a powerful tool to study protein interaction networks or molecular metabolisms. FLIM or FLIM-FRET has been used for studying molecular oncology [1–3], assessing the efficacy of cancer therapies [4, 5], the diagnosis of diseases or cellular imaging [6–8], understanding brain functions [9], image-guided surgeries [10], and characterizing fluorescent proteins or contrast agents [11, 12].

There are mainly frequency domain (FD) and time domain (TD) FLIM systems. Readers interested in FD systems, can check previously published FD systems for single-exponential [13, 14] or multi-exponential FLIM imaging [15, 16]. Typically 2~20 phase images are taken depending on applications, and usually FD FLIM software tools are iterative least squares method (LSM) based. TD time-correlated single-photon counting (TCSPC) based systems have superior signal-to-noise performance and timing resolution (down to 4ps for state-of-the-art systems) and are therefore widely considered gold-standard for FLIM-FRET applications. A typical TCSPC FLIM system contains a pulsed laser, a single-photon avalanche diode (SPAD) or a photomultiplier tube (PMT), and a TCPSC module for measuring the time delay between the detected photon and the laser pulses. In this paper, we focus on TD TCSPC based systems to develop methods of processing FLIM data. The developed methods are also applicable to time-gated systems [17, 18].

Despite the potential and significant impact of FLIM, primarily in the biological sciences, accurate estimation of fluorescence lifetimes remains a significant challenge. For live cell FLIM, it is necessary to acquire images at a frame rate fast enough to avoid motion artefacts and to resolve temporal cellular dynamics. Fortunately, recent advances in image sensors and microscopy techniques have radically boosted gold standard TCSPC-FLIM acquisition from a frame every few minutes to several frames per second [19–24]. Such significant progress makes FLIM promising for live cell imaging. However, the massive data throughput, generated by these fast imaging systems, poses a greater challenge to image analysis. For TCSPC-FLIM experiments, the time delays of detected photons are measured repeatedly, and a histogram of time delays is accumulated from which the lifetimes are to be extracted. Commercial FLIM software packages usually use LSM, such as Levenberg-Marquardt algorithms [25, 26], to calculate the true fluorescence density from the measured histogram in a pixel. This is an iterative procedure that requires users to provide an initial guess. Choosing

Optics EXPRESS

the initial guess, however, may be challenging and a LSM can easily fail to converge to a true minimum when the field of view has a wide range of lifetime contribution [27]. This explains why commercial FLIM software tools still require manual interventions from experienced users with knowledge in fluorophores and mathematical modelling to deliver a robust analysis. With analyses carried out in such supervised environments, image analysis becomes very time-consuming. A strategy that supports unsupervised analysis is really desirable.

Recently, many non-fitting algorithms have been proposed to provide fast single-exponential [28–30] or bi-exponential analysis [31–34], but they all use tail-fitting (fitting from the peak of the histogram), which assumes that the full-width at half maximum (FWHM) of the instrument response function (IRF) is negligible. They work well when the lifetime components are large, but can easily be biased when the lifetimes are comparable or even less than the FWHM of the IRF. In order to use these non-fitting algorithms robustly, high-precision (timing jitter < 50ps) detectors are required, which can significantly increase the system cost. In many applications, where the analysis speed does not matter or the fluorescence lifetimes are short, biologists still prefer fitting approaches with deconvolution that can guarantee a better performance. So far, numerous deconvolution techniques for FLIM analysis have been developed [27, 35–41]. Among them, the least squares deconvolution based on Laguerre expansion (LSD-LE) provides a fast single-exponential contrast and superior sensitivity in disease detection [38–41]. To effectively apply LSD-LE to diagnosis or parameter identification [41, 42], previous studies [40] concluded that the Laguerre basis functions (LBF) should be mutually orthogonal within the observation window (T). This requirement means T should be much larger than the largest lifetime, and it requires shining pulsed lasers with a low duty-cycle, reducing the photon collection speed. In order to avoid this constraint, we examine the LSD-LE techniques and propose to use another optimization procedure [43]. Our proposed method allows using lasers with a higher duty-cycle. Moreover, we extend LSD-LE, to our knowledge for the first time, to study bi-exponential two-photon FLIM images of the uptake of gold nanoparticles in living cells [44]. Optimized Laguerre dimension L and optimized scale α are found for bi-exponential analysis covering a wide range of lifetime distributions, supporting automated analysis.

To further guarantee unsupervised analysis, we present a simple lifetime extraction method based on a classical algorithm called the variable projection method (VPM) [43, 45]. VPM is a very useful tool for solving nonlinear least-squares problems in which a number of the parameters are linear. The VP methods have already been adopted and integrated with the global analysis method (GA) for the analysis of FLIM data [46–48]. VPM was introduced to reduce the stringent requirements on memory incurred by GA. Different from these earlier works, our approach is inspired by recent work of Barral et al. for the computation of single-exponential decays for MRI T1 relaxation imaging applications [49]. We generalize this approach to the identification of bi-exponential decays and use it to facilitate our study on the endocytosis of gold nanoparticles in living cells [6, 44, 50]. Indeed, both the single- and bi-exponential formulas are special cases of the more general VPM [45]. Nevertheless, by focusing on the bi-exponential model in particular, we derive an explicit form for the linear parameters involved in the modelling. Thus, for bi-exponential models, implementing our method is much simpler than the general VPM, which is highly desirable in a hardware implementation. We compare our simplified VPM to LSM: Our method is not only faster but also has much better photon efficiency and reliability.

The rest of this paper is organized as follows. In Section II we present our method. In Section III, our simplified VPM and LSM are tested and compared on synthesized FLIM data using tail-fitting [49] and deconvolution. Similar comparisons are carried out on various experimental FLIM data in Section IV.

Optics EXPRESS

2. Theory

2.1 Variable projection methods

We assume that the fluorescence intensity is $f(t) = K\cdot[a\cdot\exp(-t/\tau_1) + (1-a)\cdot\exp(-t/\tau_2)]$, $0 \le t \le T$, where K is the amplitude, a the proportion, τ_1 and τ_2 ($\tau_1 < \tau_2$) are the fluorescence lifetimes, and T is the observation window. Usually a TD FLIM experiment obtains a fluorescence histogram y_j, $j = 1,\ldots, N$, where y_j is the measured photon count in the j-th time bin and N is the number of time bins in a TCSPC system. Here we neglect the IRF to illustrate how VPM works (in Section 2.2 we consider the IRF). The goal of the analysis is to minimize the error

$$S(K,a,\tau_1,\tau_2) = \sum_{j=1}^{N}\left[y_j - f(t_j)\right]^2. \tag{1}$$

Here we focus on a bi-exponential model. For simplicity, we denote $A = Ka$ and $B = K(1-a)$. Instead of computing the gradient of S with respect to the unknown parameters A, B, τ_1 and τ_2, as in a traditional LSM, the error $S(A, B, \tau_1, \tau_2)$ can be rewritten as

$$\begin{aligned} S(A,B,\tau_1,\tau_2) &= A^2\sum_{j=1}^{N}e^{-2t_j/\tau_1} + B^2\sum_{j=1}^{N}e^{-2t_j/\tau_2} - 2A\sum_{j=1}^{N}y_j e^{-t_j/\tau_1} \\ &\quad - 2B\sum_{j=1}^{N}y_j e^{-t_j/\tau_2} + 2AB\sum_{j=1}^{N}e^{-t_j/\tau_1 - t_j/\tau_2} + \sum_{j=1}^{N}y_j^2 \\ &= \gamma(\tau_1)\left[A - \alpha(B,\tau_1,\tau_2)\right]^2 + \delta(\tau_1,\tau_2)\left[B - \beta(\tau_1,\tau_2)\right]^2 \\ &\quad + \eta(\tau_1,\tau_2) + \sum_{j=1}^{N}y_j^2 \end{aligned} \tag{2}$$

A simple verification of the equivalence of (2) and (1) shows that the expressions for $\gamma(\tau_1)$, $\delta(\tau_1,\tau_2)$, $\alpha(B,\tau_1,\tau_2)$, $\beta(\tau_1,\tau_2)$ and $\eta(\tau_1,\tau_2)$ equal

$$\begin{aligned} &\gamma(\tau_1) = \sum_{j=1}^{N}e^{-2t_j/\tau_1}, \\ &\delta(\tau_1,\tau_2) = \sum_{j=1}^{N}e^{-2t_j/\tau_2} - \gamma^{-1}(\tau_1)\left(\sum_{j=1}^{N}e^{-t_j/\tau_1 - t_j/\tau_2}\right)^2, \\ &\alpha(B,\tau_1,\tau_2) = \gamma^{-1}(\tau_1)\left(\sum_{j=1}^{N}y_j e^{-t_j/\tau_1} - B\sum_{j=1}^{N}e^{-t_j/\tau_1 - t_j/\tau_2}\right), \\ &\beta(\tau_1,\tau_2) = \delta^{-1}(\tau_1,\tau_2)\left[\sum_{j=1}^{N}y_j e^{-t_j/\tau_2} - \gamma^{-1}(\tau_1)\left(\sum_{j=1}^{N}y_j e^{-t_j/\tau_1}\right)\left(\sum_{j=1}^{N}e^{-t_j/\tau_1 - t_j/\tau_2}\right)\right], \\ &\eta(\tau_1,\tau_2) = -\delta(\tau_1,\tau_2)\beta^2(\tau_1,\tau_2) - \gamma^{-1}(\tau_1)\left(\sum_{j=1}^{N}y_j e^{-t_j/\tau_1}\right)^2. \end{aligned} \tag{3}$$

It is easy to prove that $\gamma(\tau_1)$ and $\delta(\tau_1,\tau_2)$ are positive. Hence minimizing $S(A,B,\tau_1,\tau_2)$ for given y_j is equivalent to

$$\begin{aligned} &(\tau_1,\tau_2) = \underset{\tau_{MIN}<\tau_1,\tau_2<\tau_{MAX}}{\text{minimize}}\left[\eta(\tau_1,\tau_2)\right], \\ &B = \beta(\tau_1,\tau_2), \quad A = \alpha(B,\tau_1,\tau_2). \end{aligned} \tag{4}$$

The advantage of these formulas, as that of those presented by Barral *et al*. for single-exponential decays [49], is that explicit expressions are given for the parameters A and B (or K and a) that appear linearly in the model. Compared with a nonlinear LSM, the likelihood of finding a global minimizer rather than a local one is much better. The VP method eliminates the linear unknowns from the least squares problem and optimizes the remaining less-dimensional least squares criterion. At the same time the problem becomes better conditioned. The eliminated linear coefficients are computed from the least squares interpolation problem after solving the optimization problem. The solution is sought from a 2-D plane within $\tau_{MIN} < \tau_1, \tau_2 < \tau_{MAX}$ (τ_{MAX} can be up to T) and users do not even need to know the exact boundaries (choosing $0 < \tau_1, \tau_2 < T$ also works well). This minimizes manual interventions and allows

Optics EXPRESS

unsupervised large FLIM data analysis. Compared with GA [51], VPM is in general faster and able to distinguish the lifetime differences for the pixels in the same segment. GA, on the other hand, is able to reduce the fitting error caused by poor SNR in a pixel. The current method and GA can be combined to provide a better SNR performance.

2.2 Calibration techniques for instrumental response functions

In a TCSPC FLIM experiment, a measured fluorescence decay $y(t)$ is the convolution of the fluorescence intensity $f(t)$ and the IRF $I(t)$:

$$y(t) = I(t) \otimes f(t) + \varepsilon(t), \quad 0 \le t \le T, \tag{5}$$

where $\varepsilon(t)$ is Poisson noise [52] and Eq. (5) can be discretized to

$$y(t_j) = \sum_{i=1}^{j} I(t_j - t_i) f(t_i) + \varepsilon(t_j), \quad j = 1, 2, ..., N. \tag{6}$$

Then the analysis when $I(j)$ is known is to minimize the error

$$S(K, a, \tau_1, \tau_2) = \sum_{j=1}^{N} \left[y_j - \sum_{i=1}^{j} I(t_j - t_i) f(t_i) \right]^2. \tag{7}$$

We can solve this curving-fitting problem directly by using the MATLAB nonlinear least-squares subroutine [25]. To facilitate our discussions, we call it C-LSM for involving convolution computations. This is the most straightforward LSM approach [51]. However, the disadvantages of C-LSM are also well-known: 1) it needs to compute convolutions for each iteration [51] and 2) it requires optimizing four parameters (K, a, τ_1, τ_2) and so expects four starting values. It is time-consuming and the analysis results are subject to the initial values [44]. To avoid the first problem above, fast deconvolutions can be used to simplify the cost function [27, 38, 40, 41, 44, 53], Eq. (7). With the deconvolution, the IRF is calibrated and an estimated $\hat{f}(t)$, and an estimated $\hat{K}$ are obtained. The normalized $\hat{f}(t)$ is similar to a filtered histogram leaving only (a, τ_1, τ_2) to be solved [44].

We recently proposed an improved fast deconvolution technique called CLSD-LE, based on Laguerre expansion [44] for analyzing bi-exponential FLIM images. But it still used traditional LSM [25, 51] to estimate (a, τ_1, τ_2), denoted as DE-LSM hereafter. VPM can be used to further reduce the dimensionality of the optimization and only (τ_1, τ_2) are to be sought. After deconvolution, an estimated $\hat{K}$ is obtained, and from Eq. (4) and the definition $B = K(1 - a)$, we find $a = 1 - \beta(\tau_1, \tau_2)/\hat{K}$. There is no need to construct or evaluate $\alpha(B, \tau_1, \tau_2)$, and we denote Eq. (4) (after conducting CLSD-LE) as DE-VPM.

3. Simulations on synthesized decays

We compared the proposed VPM and LSM using tail-fitting (TF-VPM and TF-LSM) and the improved Laguerre expansion based deconvolution methods (DE-VPM and DE-LSM) in terms of 1) the normalized bias = $\Delta g/g$, g can be a, τ_1, or τ_2 and 2) the F-value, a normalized precision defined as $F = (N_C)^{0.5} \cdot \sigma g/g$ (originally introduced for single-exponential analysis [54], but here we extended for bi-exponential models. The decovolutions were performed using CLSD-LE with the Laguerre dimension L = 16 and the Laguerre scale α = 0.912 derived by our recent studies [44]. N_C is the total count within the observation window. F = 1 for the ideal case, and $F > 1$ or $F >> 1$ for realistic FLIM analysis). Monte Carlo simulations were carried out for K = 1000 and 50, N = 256, T = 10ns, τ_2 = 2.8ns, a = 0.1, 0.37, 0.63, and 0.9, and τ_1 = 0.1, 0.37, 0.63, and 0.9ns. The IRF is assumed to have a Gaussian profile with an FWHM = 300ps.

Figures 1(a), 1(c), and 1(e) show the normalized bias plots, whereas Figs. 1(b), 1(d), and 1(f) show the F plots, for a, τ_1, and τ_2 respectively. Figures 1(a) and 1(c) indicate that tail-

Optics EXPRESS

fitting actually causes biased estimations of a and τ_1 (apart from τ_2) when τ_1 is small. In applications where the information of a or τ_1 is essential, using tail-fitting (TF-LSM or TF-VPM) can lead to misinterpretation of data. However, if the information of τ_2 is sought after, then the TF-VPM analysis can provide acceptable bias performances ($\Delta\tau_2/\tau_2$ < 10%) and precision performances that are comparable to the DE-LSM analysis. In comparison with DE-LSM and DE-VPM, C-LSM has comparable or better bias performances only when the initial values are well chosen. Figure 1 shows DE-VPM's superior performances in photon efficiency. Apart from the extreme case a = 0.1 and τ_1 = 0.1ns, the normalized bias is in general less than 10% and the F-value less than 10, showing that it has the best photon efficiency among the five approaches. Note that for synthesized FLIM data it is easy to set the initial values for LSM, as a, τ_1, and τ_2 are already known. In cases where the field of view has a wide range of variations, LSM is not able to converge robustly to the true minima and its output depends on the given starting values. Compared with DE-VPM, the dynamic range of DE-LSM is very limited, and it only provides comparable performances when $\tau_2 >> \tau_1$.

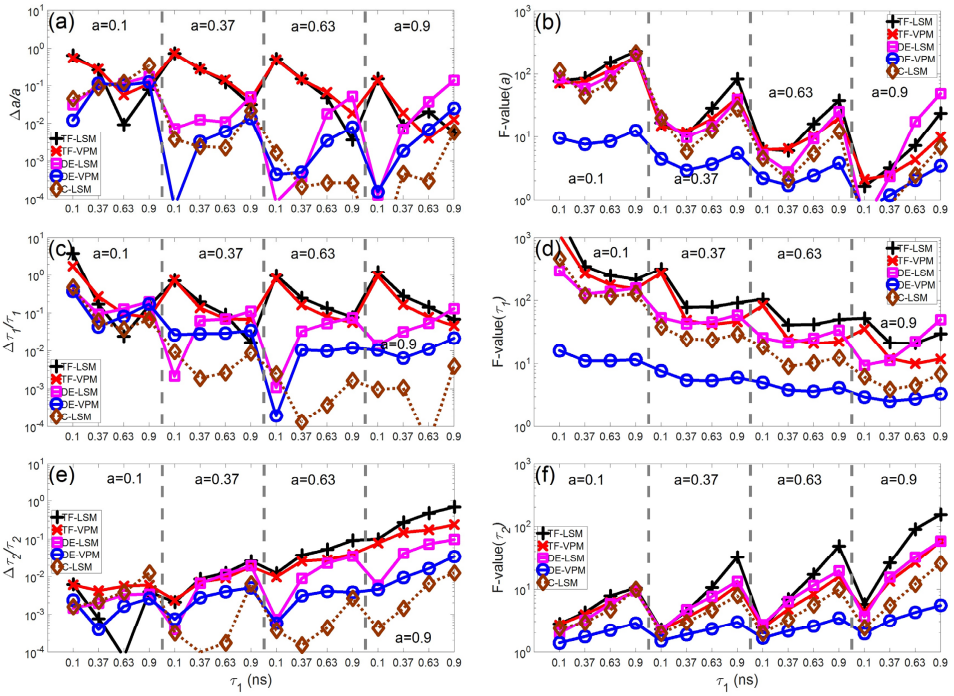

Fig. 1. (a), (c), and (e), Bias and (b), (d), and (f) F plots for different methods, K = 1,000, and N = 256.

Figures 2(a)-2(f) show the bias and F-value plots using the same settings as above but with K = 50. The purpose of this analysis is to demonstrate the performance of the proposed approach when the photon count is low. This happens in some live-cell imaging or high-throughput screening applications where the acquisition has to be short [10, 55]. Again, the TF analysis produces more biased estimations when τ_1 is small. At a low count, it is difficult to use any method to estimate a accurately when a is small, as shown in Fig. 2(a). Among C-LSM, DE-LSM, and DE-VPM, C-LSM has better performances in $\Delta\tau_1/\tau_1$, whereas DE-LSM and DE-VPM have better performances in $\Delta\tau_2/\tau_2$. Figures 2(b), 2(d), and 2(f) show similar F plots to Figs. 1(b), 1(d), and 1(f). The F-values of TF-LSM, TF-VPM, C-LSM, and DE-LSM are comparable, and they are in general larger than that of DE-VPM ($F_{\text{DE-VPM}}$ < 10).

Optics EXPRESS

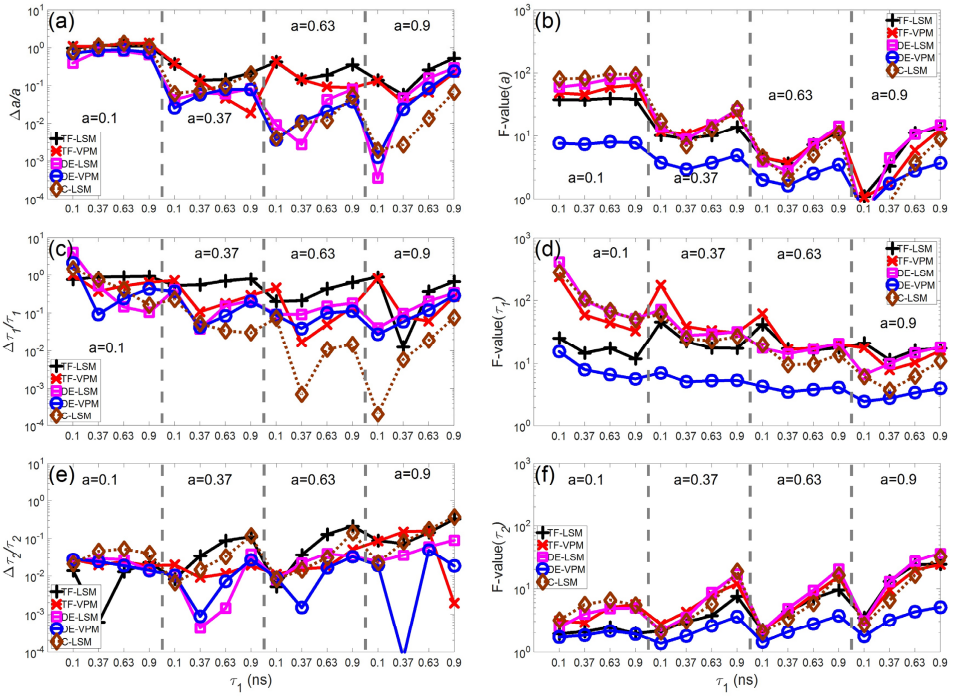

Fig. 2. (a), (c), and (e) Bias and (b), (d), and (f) F plots for different methods, K = 50, and N = 256.

In terms of the analysis speed, Table 1 shows the average fitting time of 16 decays for different a and τ_1 (a = 0.1, 0.37, 0.63, and 0.9, τ_1 = 0.1, 0.37, 0.63, and 0.9ns) for different methods. Simulations were carried out using MATLAB® R2015b on a Dell PrecisionM2800 (Intel Core i7-4810MQ CPU @ 2.80GHz, 16.0 GB memory; OS: Windows 7 Enterprise Service Pack 1 64-bit). The table shows that our VPM requires less time than LSM. The simulation time of C-LSM varies significantly depending on the initial values. In realistic scenarios, it is difficult to obtain accurate initial guesses. On the other hand, our VPM does not suffer this problem. It converges robustly at a faster speed, regardless of the initial values and therefore promising for automated analysis. It is surprising that TF-LSM takes more time than DE-LSM, but it is reasonable as more iterations are required for TF-LSM to obtain convergent results when the IRF is neglected.

Table 1. Average fitting time of 16 decays for different methods.

Methods	K = 1000 (sec)	K = 50 (sec)
TF-LSM	0.144	0.199
TF-VPM	0.087	0.091
DE-LSM	0.136	0.188
DE-VPM	0.105	0.121
C-LSM	0.339*	0.362*

*The initial values need to be within (1 ± 20%) × the real values.

In some applications, such as estimating the efficiency of FRET transfer, the amplitude-averaged lifetime $\tau_{ave} = a\tau_1 + (1-a)\tau_2$ is to be estimated [37]. Figure 3 shows the normalized bias and F plots of τ_{ave} using K = 1000 and K = 50. Figure 3(a) shows that TF-LSM and TF-VPM produce comparable estimations, but it also indicates the need to consider the IRF to avoid biased estimations. In general, DE-VPM performs better in the bias ($\Delta\tau_{ave}/\tau_{ave} < 2\%$) and photon efficiency (F–value). DE-LSM only provides comparable precision when τ_1 is small. Similarly, for K = 50, Fig. 3(c) indicates that the IRF needs to be considered in lifetime

Optics EXPRESS

estimations. Without deconvolution, the TF analysis produces the most biased estimations when τ_1 = 0.1ns. Considering both the bias and the precision for different K, DE-VPM does offer a wider dynamic range and superior photon efficiency.

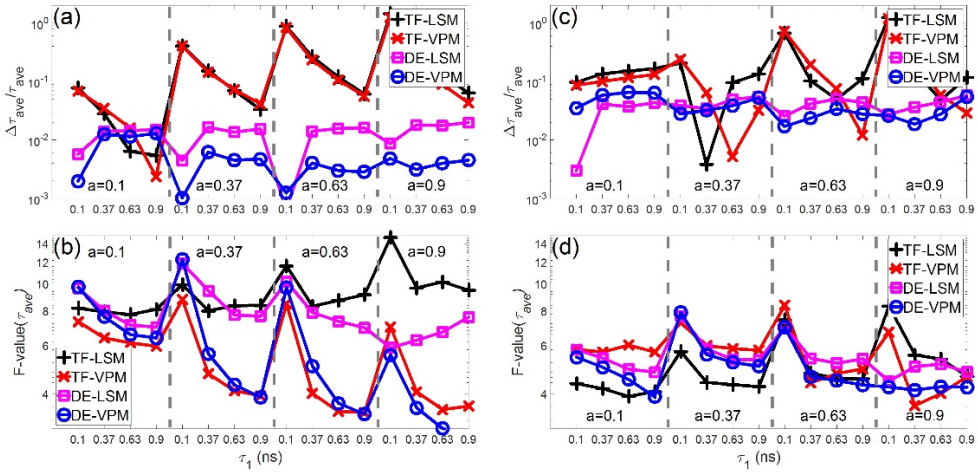

Fig. 3. (a) Normalized bias and (b) F plots for $\tau_{ave} = a\tau_1 + (1- a)\tau_2$ when K = 1000. (c) Normalized bias and (d) F plots for τ_{ave} when K = 50.

4. Experimental results

4.1 Daisy pollen

The first example is to study the fluorescence lifetimes of the autofluorescence emitted from daisy pollen. Autofluorescence of biological samples as well as the fluorescence lifetime can be very useful. For example, cellular autofluorescence is used as a good label-free indicator for studying cytotoxicity [56]. The FLIM data are obtained using the MicroTime 200 (PicoQuant), equipped with the standard piezo scanner from Physik Instrumente (100x100μm scan range) and a Hybrid-PMT (PMA Hybrid-40). The TCSPC system used for the acquisition is the HydraHarp 400 with the bin width set to 8ps and each histogram contains 6253 time bins (the equivalent full range = 50ns). Other parameters include: excitation wavelength = 485nm, the laser repetition rate = 20 MHz (LDH-D-C-485 laser head controlled by the PDL 828 "Sepia II" laser driver) and the detection band = 520/35.

Figure 4 shows the measured IRF, measured and fitted histograms (using DE-VPM) at the brightest pixel, and the summed histogram of all pixels. The FWHM of the IRF is around 300ps; it is much larger than τ_1. Traditional tail-fitting practices can easily overestimate τ_1 and even τ_2 [57]. Therefore, deconvolutions of the IRF should be performed to accurately determine lifetimes.

Optics EXPRESS

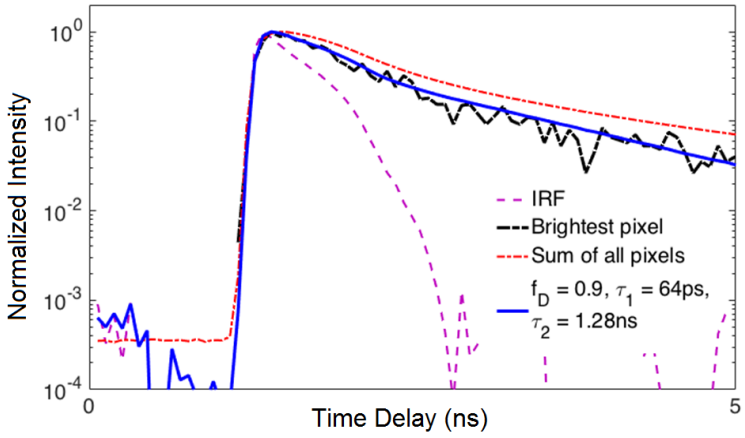

Fig. 4. Measured IRF, measured and fitted histograms.

Figures 5(a)-5(d) show the fluorescence intensity, $\tau_{ave} = a\tau_1 + (1-a)\tau_2$, a and τ_2 images, respectively, obtained by DE-VPM. They clearly show the differences between the intensity and lifetime maps. The fraction, a, within the pollen is close to 1, showing that there is near single-exponential fast autofluorescence (smaller τ_{ave}). The fraction is smaller on the spikes, but it is in general larger than 0.5, see the blue open-circle curve in Fig. 5(e). The results are very different from those obtained by tail-fitting reported in the literature [57, 58]. To compare the differences between LSM and VPM as well as the impact of the IRF on the lifetime estimations, we also perform the analysis using TF-LSM, TF-VPM, DE-LSM, and DE-VPM. Figures 5(e)-5(h) show the a, τ_2, τ_1 (note that this is in log scale), and τ_{ave} histograms, respectively. The figures indicate that neglecting the IRF for the TF analysis does bias all parameters and make the estimations sensitive to the observation window. Usually for tail- fitting the observation window starts from the peak of the histogram or a certain distance away from the peak [57]. However, the peak position is noise inflicted and difficult to be determined precisely when the photon count is low. Tail-fitting approaches (both TF-LSM and TF-VPM) underestimate a and τ_1 and overestimate τ_2 and τ_{ave}. TF-LSM and TF-VPM show similar analyses except that TF-VPM is superior in photon efficiency and it is able to resolve low-count pixels showing $\tau_1 > 0.1$ns. The figures also show the advantages of the proposed DE-VPM. Instead of searching the optimized solution in a 3-D (a, τ_1, τ_2) space as traditional LSM approaches, the VPM identifies it in a 2-D (τ_1, τ_2) space. As mentioned earlier, our VPM does not need a precise initial guess and a rough range [8ps, 10ns] suffices to guarantee consistent analysis results. For DE-LSM, on the other hand, it usually requires a good guess (from an experienced user) for a satisfactory analysis. In this figure, a starting value ($a = 0.9$, $\tau_1 = 0.05$ns, $\tau_2 = 1$ns; pink open square curve) close to the real distribution and a randomly chosen one ($a = 0.1$, $\tau_1 = 0.5$ns, $\tau_2 = 2$ns; green open square curve) were given to illustrate this issue. Figure 5(f) shows that an ill-chosen initial guess ($a = 0.1$, $\tau_1 = 0.5$ns, $\tau_2 = 2$ns) prompts the search process for a significant amount of pixels to converge to a local minimum and therefore obtain biased estimations $\tau_2 < 0.1$ns. When the starting value is well chosen, DE-LSM can obtain results coinciding with those of DE-VPM apart from some biased estimations at pixels with a lower photon count (pointed to by the pink arrow). As discussed earlier, Fig. 5(g) shows that the TF approaches obtain biased τ_1, even much smaller than the timing resolution of the TCSPC (8ps) at most pixels. For the DE analysis, many pixels fail to converge for the DE-LSM analysis with the initial values $a = 0.1$, $\tau_1 = 0.5$ns, $\tau_2 = 2$ns. Figure 5(h) shows that the ill-chosen initial values produce a slightly different τ_{ave} histogram from the DE-VPM and the DE-LSM results with a well-chosen initial guess. Again, TF-LSM and TF-VPM produce similar results, but they both overestimate τ_{ave}.

Optics EXPRESS

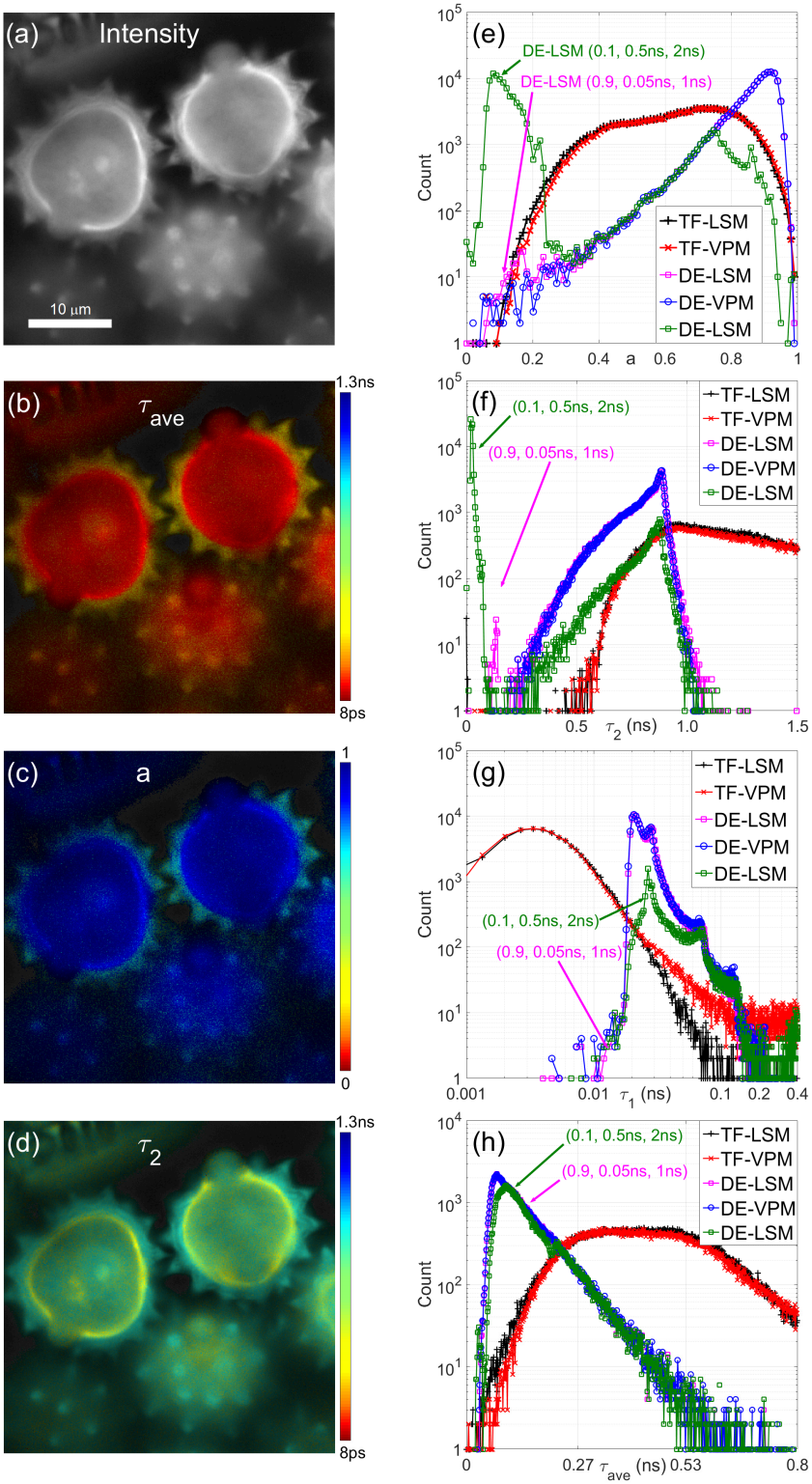

Fig. 5. (a) Intensity, (b) τ_{ave}, (c) a, and (d) τ_2 images; (e) *a*, (f) τ_2, (g) τ_1, and (h) τ_{ave} histograms. obtained by DE-VPM.

Optics EXPRESS

4.2 Two-photon FLIM images of gold nanoparticles in live cells

Gold nanoparticles (GNP) show tunable localized surface plasmon resonance, superior quenching capability and low toxicity. These unique properties allow efficient energy transfer between fluorophores and gold nanoparticles and hence provide a new paradigm for developing novel molecular probes or contrast agents [6, 59–61]. However, factors that affect the uptake of GNPs in cells, such as dose, GNP shape and surface functionalization, cell types, and distributions of GNPs in cells, have not been fully characterized yet. Fully decoding the impacts of these factors requires a massive amount of raw data obtained from different FLIM experiments, and therefore it is desirable to have a faster analysis approach.

The proposed VPM can be used to analyze FLIM images of Cy5-ssDNA-gold-nanorod (GNR) labelled Hek293 cells for assessing the uptake of GNR in cells. The procedures for synthesizing GNR-based RNA nanoprobes can be found in [6]; in brief, GNRs were functionalized with thiolated oligonucleotides (ssDNA) labelled with Cy5 through ligand exchange and salting aging process. After the incubation with Cy5-ssDNA-GNRs, Hek293 cells were washed and fixed with paraformaldehyde. Two-photon FLIM experiments were performed on a confocal microscope (LSM 510, Carl Zeiss) with a SPC-830 TCSPC card (Becker & Hickl GmbH). Laser excitation pulses (200 fs) with a repetition rate of 80MHz were generated from a Chameleon Ti:sapphire laser (Coherent). The bin width of the TCSPC is set to be 0.039ns, and each measured histogram contains 256 time bins (therefore the equivalent full range $T = 256 \times 0.039 = 10$ns).

Figures 6(a) and 6(b) show the amplitude-average lifetime, $\tau_{ave} = a\tau_1 + (1–a)\tau_2$, and a images obtained by DE-VPM. The decovolutions were performed using the enhanced CLSD-LE with $L = 16$ and $\alpha = 0.912$ [44]. Different from traditional fluorescence intensity imaging, FLIM images, Figs. 6(a)-6(c), offer much more information and are able to identify the locations of GNRs (at pixels showing $\tau_1 < 100$ps; τ_1 is the fluorescence lifetime of GNRs, in good agreement with previously published results [6]). Together with the lifetime histograms, Fig. 6(c)-6(f) can further assess whether there are improperly folded probes on GNRs [6]. Figure 6(d) show τ_1, τ_2 and τ_{ave} histograms as a function of a, and Fig. 6(e) shows the lifetime-intensity histograms. The τ_{ave} histogram (< 2ns) shown in Fig. 6(d) can also be obtained from single-exponential analysis [29]. However, single-exponential models are not able to distinguish between the fluorescence from GNR probes and the autofluorescence from cells. The τ_2 histograms in Figs. 6(d) and 6(e) show two clusters of pixels: 1) the cluster in light blue dots; and 2) the cluster in deep blue dots. The low fluorescence intensity (< 1500), Fig. 6(e), detected at most pixels in the first cluster, is likely due to the autofluorescence (with $\tau_1 >$ 0.1ns and $\tau_2 > 2.0$ns). On the other hand, the existence of short τ_1 (< 100ps) indicates that Cy5 is in the quenched state. Most pixels in the second cluster show $a > 0.6$ and $\tau_2 = 2.0 \pm 0.2$ns (in good agreement with previously published reports [62]) with the brightest cluster (in red open circles) showing larger a and smaller τ_2 values, suggesting stronger energy transfer between GNRs and Cy5 at these pixels, see the τ_2 map at the GNRs with $a > 0.95$ in Fig. 6(c). This experiment demonstrates the importance to have a robust and fast analysis tool that is capable of extracting small τ_1 (much less than the FWHM of the IRF) accurately.

Optics EXPRESS

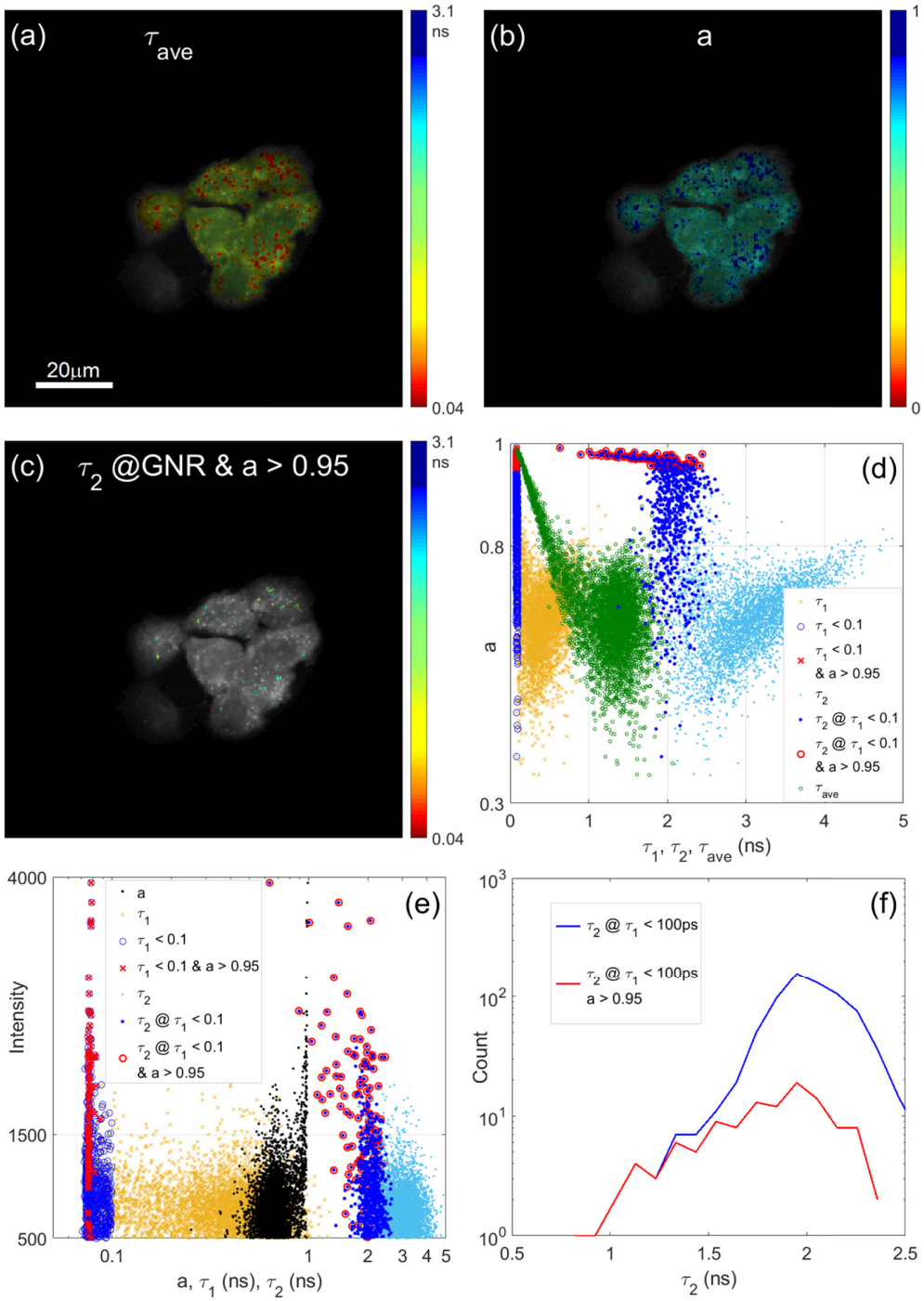

Fig. 6. (a) τ_{ave} map, (b) a map, (c) τ_2 map at the pixels showing τ_2 < 100ps and a > 0.95, (d) lifetime (τ_1,τ_2, τ_{ave}) vs a histograms showing one brighter cluster with τ_1 < 100ps and 2.0 < τ_2 < 4.4ns and one dimmer cluster with 100ps <τ_1 < 1.2ns and 0.5 < τ_2 < 2.5ns, (e) intensity vs (a,τ_1, τ_2) histograms indicate that the brighter pixels have shorter τ_2 and higher a (suggesting Cy5 is strongly quenched).

Optics EXPRESS

5. Conclusion

We propose a fast bi-exponential FLIM algorithm based on variable projection, inspired by a recently published work on MRI T1 relaxation imaging [49]. There are two advantages: 1) our VPM only performs 2-D (τ_1, τ_2) minimization instead of 3-D (a, τ_1, τ_2) or 4-D (K, a, τ_1, τ_2) optimization required in most LSM-based FLIM analysis tools. It is therefore more robust and faster. Moreover, in our applications it does not require to estimate initial values, which is promising for automated analysis. 2) our VPM shows much higher photon efficiency than traditional LSM approaches. To characterize the IRF, we combine our VPM with our new Laguerre expansion deconvolution method [44], DE-VPM. DE-VPM was tested on both synthesized and experimental FLIM data (daisy pollen), showing that DE-VPM outperforms DE-LSM in terms of accuracy, speed and photon efficiency. High photon efficiency is particularly useful, because it means that much fewer photons are required for DE-VPM to provide similar precision as LSM based tools. DE-VPM analysis was also tested on the FLIM images of Cy5-ssDNA-GNR labelled Hek293 cells and output comparable results with previously published literature. DE-VPM seems to be promising for FLIM applications that produce large amounts of data or that require fast FLIM analysis.

Funding

The Royal Society (IE140915); Biotechnology and Biological Sciences Research Council (BBSRC) (BB/K013416/1).

Acknowledgments

The authors would like to acknowledge China Scholarship Council, Research Foundation – Flanders (FWO), G. Wei, J. Sutter, W. Li, and R. Y. M. M. Qotob for supporting this work. We would also like to thank Dr. Andreas Bülter and Dr. Volker Buschmann, PicoQuant, Germany, for their technical support.